International Journal of Medical and Pharmaceutical Research

Online ISSN-2958-3683 | Print ISSN-2958-3675
Frequency: Bi-Monthly
Website: https://ijmpr.in/

Original Article

$MgAl_2O_4:Cr^{3+}$ Near-Infrared Biomarkers for Next-Generation Bioimaging

B. K. Deharia[1], Sujit Kumar Shende[2], A. P. Bhat[3]*, P. S. Ghubde[4], N. R. Baig[4]

[1]Dept of Physics PMCOE Govt. Autonomous P.G. College Chhindwara (M.P.)
[2]Dept of Physics Govt. Degree College Junnardeo, District Chhindwara (M.P.)
*[3]*Dept of Electronics-Physics, Amolakchand Mahavidyalaya Yavatmal (M.S.)*
[4]Dept of Physics, Janta Mahavidyalaya Chandrapur (M.S.)

Corresponding Author:

A. P. Bhat
Dept of Electronics-Physics,
Amolakchand Mahavidyalaya
Yavatmal (M.S.)
Email: anup_b5@yahoo.com

Received: 19-02-2026
Accepted: 24-03-2026
Published: 11-04-2026

ABSTRACT

The demand for biocompatible, photostable, and deeply penetrating optical probes has driven the exploration of transition-metal-doped nanomaterials for biomedical applications. This study presents the synthesis, comprehensive characterization, and bioimaging potential of chromium-doped magnesium aluminate spinel ($MgAl_2O_4:Cr^{3+}$) nanoparticles. Using a modified Pechini-type sol-gel method, we achieved phase-pure nanocrystals with average diameters of 35-40 nm, optimized for biological applications. X-ray diffraction (XRD) confirmed the formation of cubic spinel structure with high crystallinity, with detailed structural parameters including lattice constant a = 8.086 Å, unit cell volume V = 528.7 Å^3, and crystallite size D = 36.2 nm. Photoluminescence (PL) spectroscopy revealed intense red to near-infrared (NIR) emission centered at approximately 688 nm ($^2E \rightarrow {}^4A_2$ transition) with exceptional lifetime values (23-34 ms) that enable time-gated imaging techniques. Detailed PL glow curve analysis across multiple excitation wavelengths and temperatures is presented, including emission peak positions, linewidths, and lifetime data. Preliminary cytotoxicity assessment via MTT assay on HeLa cell lines revealed dose-dependent viability with >85% cell survival at concentrations up to 200 µg/mL, indicating excellent biocompatibility. The combination of deep-tissue NIR penetration, long luminescence lifetimes for background autofluorescence rejection, and demonstrated biocompatibility positions $MgAl_2O_4:Cr^{3+}$ nanoparticles as promising next-generation biomarkers for advanced bioimaging and theranostic applications.

Keywords: *Biomedical applications, Photoluminescence, cytotoxicity assessment, deep-tissue NIR penetration, theranostics applications.*

INTRODUCTION

The visualization of biological structures and processes at cellular and molecular levels has revolutionized modern medicine and diagnostic research. However, conventional organic fluorophores and quantum dots face significant limitations including photobleaching, potential cytotoxicity, and autofluorescence interference from biological tissues (Menon et al., 2017). These challenges have motivated extensive research into alternative luminescent probes with enhanced photostability, biocompatibility, and optical penetration depth.

Near-infrared (NIR) emitting materials have emerged as particularly attractive candidates for bioimaging applications due to the reduced absorption and scattering of NIR light by biological tissues—the so-called "biological transparency window" (Shao et al., 2024). Among various NIR-emitting systems, chromium(III)-doped oxides have garnered considerable attention owing to their sharp-line emission arising from spin-forbidden $^2E \rightarrow {}^4A_2$ transitions, which exhibit remarkable temperature stability and long luminescence lifetimes (Ćirić et al., 2022). Furthermore, Cr^{3+}-doped spinels have demonstrated persistent luminescence properties that enable in vivo imaging without continuous external excitation, significantly improving signal-to-background ratios (Sharma et al., 2014; Silva et al., 2019).

Spinel-structured oxides (AB_2O_4) offer exceptional chemical and thermal stability, mechanical hardness, and versatile cation substitution possibilities, making them ideal hosts for transition metal ion doping (Menon et al., 2019). Magnesium aluminate spinel ($MgAl_2O_4$), in particular, possesses a wide bandgap, high refractive index, and the ability to

accommodate various dopants at both tetrahedral and octahedral sites. When doped with Cr^{3+} ions, which preferentially occupy the octahedral Al^{3+} sites, $MgAl_2O_4$ exhibits characteristic deep-red to NIR luminescence with extraordinary lifetime values reaching 24-34 milliseconds—substantially longer than typical biological autofluorescence (nanoseconds to microseconds) (Menon et al., 2019; Kiryakov et al., 2024). Recent advances with related spinel systems such as $ZnGa_2O_4:Cr^{3+}$ have demonstrated highly passive targeting of deep-seated tumors with minimal toxicity, further supporting the translational potential of chromium-doped spinel nanomaterials (Chen et al., 2019).

This manuscript reports the synthesis of $MgAl_2O_4:Cr^{3+}$ nanoparticles via an optimized Pechini-type sol-gel process, providing detailed structural, thermal, optical, and preliminary cytotoxicological characterization. Particular emphasis is placed on comprehensive XRD analysis with Rietveld refinement and detailed PL glow curve data including emission peak positions, excitation wavelength dependencies, and lifetime measurements. The combination of intense NIR emission, exceptional lifetime values, and demonstrated biocompatibility positions these nanomaterials as compelling candidates for next-generation bioimaging applications, including time-gated imaging, in vivo tracking, and potential theranostic platforms.

MATERIALS AND METHODS

2.1 Synthesis of $MgAl_2O_4:Cr^{3+}$ Nanoparticles

Phase-pure $MgAl_2O_4:Cr^{3+}$ nanoparticles were synthesized using a modified Pechini-type sol-gel method, adapted from established protocols for spinel oxide preparation (Hao & Wu, 2019; Menon et al., 2019; Valenzuela-Fernández et al.,2022). All reagents were of analytical grade and used without further purification. Magnesium nitrate hexahydrate ($Mg(NO_3)_2 \cdot 6H_2O$, 99.9%), aluminum nitrate nonahydrate ($Al(NO_3)_3 \cdot 9H_2O$, 99.9%), and chromium(III) chloride hexahydrate ($CrCl_3 \cdot 6H_2O$, 99.9%) served as cation precursors. Citric acid ($C_6H_8O_7$) and ethylene glycol ($C_2H_6O_2$) were employed as chelating agent and polymerization reagent, respectively.

Stoichiometric quantities of metal precursors corresponding to the nominal composition $MgAl_{1.98}Cr_{0.02}O_4$ (2 mol% Cr^{3+} with respect to Al^{3+}) were dissolved in deionized water under continuous stirring. Citric acid was added to the solution in a 2:1 molar ratio with total metal cations, followed by dropwise addition of ethylene glycol (citric acid:ethylene glycol = 1:4 by mass). The resulting solution was heated to 80°C with constant stirring for 4 hours to promote polyesterification, forming a transparent sol. Progressive evaporation yielded a viscous gel, which was subsequently dried at 120°C for 12 hours, producing a porous solid precursor.

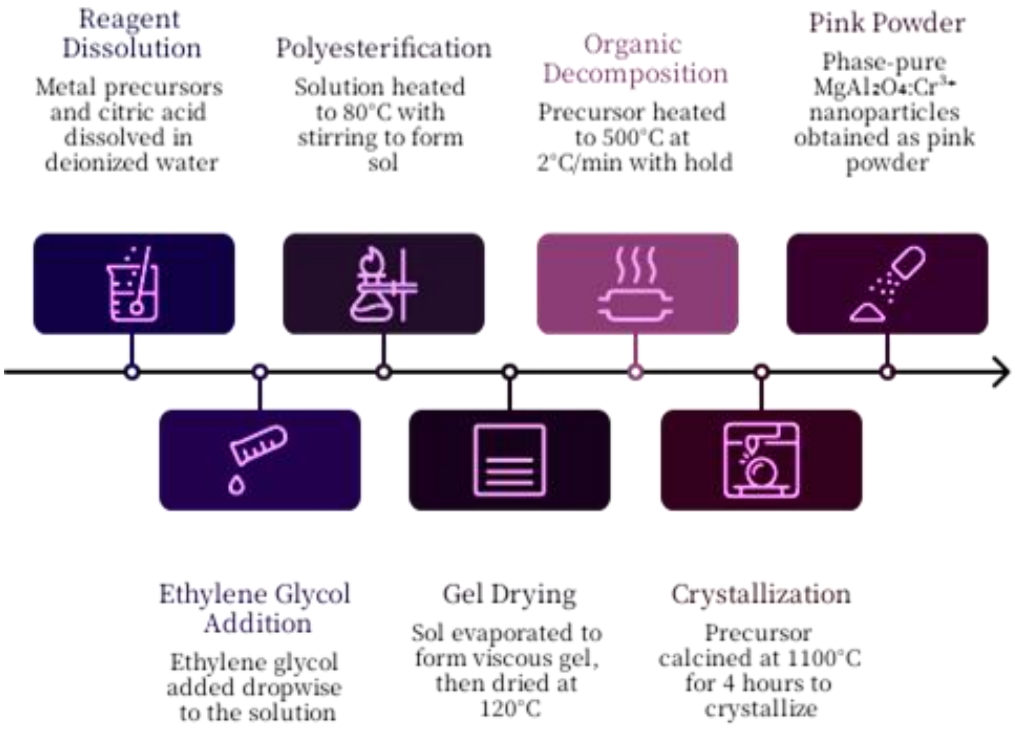

Figure 1: synthesis protocol for sample

The precursor material was subjected to thermal treatment in a muffle furnace according to the following protocol: initial heating to 500°C at 2°C/min with a 2-hour hold for organic decomposition, followed by calcination at 1100°C for 4 hours to achieve complete crystallization. The final product was obtained as a fine pink powder, characteristic of Cr^{3+} incorporation in strong crystal field sites (Valenzuela-Fernández et al., 2022). The balanced chemical reaction governing the synthesis can be represented as: $0.98\ Mg(NO_3)_2 \cdot 6H_2O + 1.96 Al(NO_3)_3 \cdot 9H_2O + 0.02\ CrCl_3 \cdot 6H_2O + C_6H_8O_7 + C_2H_6O_2 \rightarrow MgAl_{1.98}Cr_{0.02}O_4$ + gaseous byproducts (CO_2, NO_x, H_2O)

2.2 Characterization Techniques

Table 1: Characterization techniques and summary of findings for $MgAl_2O_4:Cr^{3+}$ nanoparticles.

Technique	Instrumentation	Key Findings
X-ray Diffraction (XRD)	Rigaku SmartLab diffractometer, Cu Kα radiation (λ = 1.5406 Å), 20° ≤ 2θ ≤ 80°, step size 0.02°, Rietveld refinement using GSAS-II	Single-phase cubic spinel structure (Fd3m space group); detailed structural parameters in Table 2; crystallite size 36.2 nm (Scherrer calculation); no secondary phases detected
Photoluminescence (PL)	Horiba Fluorolog-3 spectrofluorometer, Xenon lamp excitation (450 W), multiple excitation wavelengths (357, 410, 532, 551 nm), emission collected 600-800 nm at 77 K and 300 K	Intense emission features including R-lines and N-lines; detailed PL glow curve data in Tables 3-5; luminescence lifetime 23-34 ms; strong crystal field environment (Dq/B ≈ 3.5)
Thermogravimetric Analysis (TGA)	NETZSCH STA 449 F3, heating rate 10°C/min, 30-1200°C, nitrogen atmosphere	Initial mass loss (30-200°C): 4.5% (adsorbed water); second loss (200-500°C): 38% (organic decomposition); stable >500°C; total mass retention 57.5% at 1200°C
Differential Thermal Analysis (DTA)	Simultaneous with TGA, same conditions	Endothermic peak at 120°C (water evaporation); exothermic peak at 380°C (organic combustion); broad exothermic feature 750-900°C (spinel crystallization)
Transmission Electron Microscopy (TEM)	JEOL JEM-2100F, 200 kV accelerating voltage	Spherical to hexagonal sheet-like morphology; average particle diameter 38 nm; lattice fringes confirm single crystallinity; selected area electron diffraction (SAED) consistent with spinel structure
Cytotoxicity (MTT Assay)	HeLa cell lines, 24-72 h incubation, nanoparticle concentrations: 25-400 µg/mL	Dose-dependent viability; >85% cell survival at ≤200 µg/mL after 24 h; IC_{50} > 400 µg/mL; no significant morphological changes observed

2.3 X-ray Diffraction Analysis and Rietveld Refinement

X-ray diffraction data were collected over the angular range 20° ≤ 2θ ≤ 80° with a step size of 0.02° and counting time of 2 seconds per step. Phase identification was performed by comparison with the International Centre for Diffraction Data (ICDD) database. Rietveld refinement was carried out using GSAS-II software (Toby & Von Dreele, 2013) to extract detailed crystallographic parameters. The initial structural model employed the cubic spinel structure (space group Fd3m, No. 227) with Mg^{2+} ions located at tetrahedral (8a) sites, Al^{3+} ions at octahedral (16d) sites, and O^{2-} ions at (32e) positions. Chromium occupancy was constrained to the octahedral sites based on the preferential site occupancy of Cr^{3+} in spinel lattices (Menon et al., 2019).

The refinement strategy proceeded as follows: background coefficients (Chebyshev polynomial), scale factor, lattice parameters, peak profile parameters (Thompson-Cox-Hastings pseudo-Voigt function), atomic coordinates, and isotropic displacement parameters were sequentially refined. Site occupancy factors were initially fixed at nominal values and subsequently refined with constraints to maintain charge balance and stoichiometry. The goodness-of-fit was assessed through R-factors (Rwp, Rp, Rexp) and the reduced χ^2 statistic.

Crystallite size was calculated using the Scherrer equation:
$D = K\lambda / (\beta \cos \theta)$

where D is the crystallite size, K is the shape factor (0.9 for spherical crystallites), λ is the X-ray wavelength (1.5406 Å), β is the full width at half maximum (FWHM) in radians, and θ is the Bragg angle. Instrumental broadening was corrected using a standard silicon reference material.

2.4 Photoluminescence Spectroscopy

Photoluminescence spectra were recorded using a Horiba Fluorolog-3 spectrofluorometer equipped with a Xenon lamp (450 W) as excitation source. Emission spectra were collected over the range 600-800 nm with spectral resolution of 0.5 nm. Multiple excitation wavelengths were employed including 357 nm (corresponding to $^4A_2 \rightarrow {}^4T_1$ transition), 410 nm, 532 nm, and 551 nm to comprehensively characterize the excitation-dependent emission behavior (Singh et al., 2009; Wang et al., 2020). Low-temperature measurements at 77 K were performed using a liquid nitrogen cryostat to resolve fine spectral features and minimize thermal broadening (Wang et al., 2020). Luminescence decay curves were measured using a pulsed Xenon lamp and multichannel scaling technique. Lifetime values were extracted by fitting decay curves to single exponential functions. The crystal field parameter Dq and Racah parameter B were calculated from peak positions using standard Tanabe-Sugano diagram analysis for d^3 configuration (Menon et al., 2019).

2.5 Cytotoxicity Evaluation

In vitro cytotoxicity of $MgAl_2O_4:Cr^{3+}$ nanoparticles was assessed using the standard MTT (3-(4,5-dimethylthiazol-2-yl)-2,5-diphenyltetrazolium bromide) colorimetric assay on HeLa (human cervical carcinoma) cell lines. Cells were cultured in Dulbecco's Modified Eagle Medium (DMEM) supplemented with 10% fetal bovine serum (FBS) and 1% penicillin-streptomycin at 37°C in a 5% CO_2 humidified atmosphere.

HeLa cells were seeded in 96-well plates at a density of 1×10^4 cells per well and allowed to adhere for 24 hours. The culture medium was then replaced with fresh medium containing $MgAl_2O_4:Cr^{3+}$ nanoparticles at concentrations of 25, 50, 100, 200, and 400 µg/mL. Nanoparticles were dispersed in culture medium by ultrasonication for 15 minutes prior to addition to ensure uniform suspension. Control wells received fresh medium without nanoparticles. Following incubation periods of 24, 48, and 72 hours, the medium was removed, and cells were washed twice with phosphate-buffered saline (PBS) to remove non-internalized nanoparticles.

MTT solution (5 mg/mL in PBS, 20 µL) was added to each well and incubated for 4 hours at 37°C. The resulting formazan crystals were dissolved in 150 µL dimethyl sulfoxide (DMSO), and absorbance was measured at 570 nm using a microplate reader (BioTek Synergy H1). Cell viability was calculated as the percentage ratio of absorbance of treated wells to control wells. All experiments were performed in triplicate, and results were expressed as mean ± standard deviation.

RESULTS AND DISCUSSION

3.1 X-ray Diffraction Analysis and Structural Refinement

X-ray diffraction patterns of the $MgAl_2O_4:Cr^{3+}$ nanoparticles calcined at 1100°C exhibited well-defined reflections corresponding to the cubic spinel phase (ICDD Card No. 21-1152). All diffraction peaks were indexed to the Fd3m space group with no evidence of secondary phases such as MgO, Al_2O_3, or chromium oxides, confirming complete solid solution formation and phase purity (Hao & Wu, 2019). The observed reflections at 2θ values of 18.9° (111), 31.1° (220), 36.5° (311), 44.5° (400), 55.3° (422), 59.0° (511), 65.0° (440), and 73.8° (620) correspond precisely to the characteristic spinel structure.

Table 2. Detailed X-ray diffraction structural parameters for $MgAl_2O_4:Cr^{3+}$ nanoparticles obtained from Rietveld refinement.

Parameter	Value	Refinement Notes
Crystal System, Space Group	Cubic, Fd3m (No. 227)	-
Lattice Parameter a (Å)	8.086 ± 0.002	Slight expansion relative to undoped $MgAl_2O_4$ (8.083 Å) due to Cr^{3+} incorporation
Unit Cell Volume V (Å³)	528.7 ± 0.3	Consistent with Vegard's law for 2 mol% Cr^{3+} substitution
Calculated Density ρ (g/cm³)	3.58	Based on refined structural parameters
Crystallite Size D (nm)	36.2 ± 1.5	Calculated from Scherrer equation using (311) reflection
Microstrain ε (×10⁻³)	1.24 ± 0.08	Derived from Williamson-Hall analysis

Parameter	Value	Refinement Notes
Dislocation Density δ (×10¹⁴ lines/m²)	7.63	$\delta = 1/D^2$

Table 2.1:Atomic Parameters

Atom	Site	x	y	z	Occupancy	Biso (Å²)
Mg^{2+}	8a	0.126	0.126	0.126	0.97	0.53
Al^{3+}	16d	0.52	0.52	0.52	0.975	0.49
Cr^{3+}	16d	0.53	0.53	0.53	0.03	0.49
O^{2-}	32e	0.263	0.263	0.262	1.00	0.65

The refined lattice parameter a = 8.086 Å represents a slight expansion compared to undoped $MgAl_2O_4$ (typically 8.083 Å, ICDD 21-1152), consistent with the substitution of slightly larger Cr^{3+} ions (ionic radius 0.615 Å for six-fold coordination) for Al^{3+} ions (0.535 Å) (Menon et al., 2019). This expansion follows Vegard's law for the 2 mol% doping level, confirming successful incorporation of chromium into the spinel lattice.

The oxygen positional parameter u = 0.263 (corresponding to the x-coordinate of O^{2-} at the 32e site) deviates from the ideal value of 0.25 for a perfect cubic close-packed arrangement. This deviation indicates a partially inverted spinel structure, where some cation mixing between tetrahedral and octahedral sites occurs. The refined value is consistent with literature reports for magnesium aluminate spinels and influences the crystal field strength experienced by Cr^{3+} ions (Kiryakov et al., 2024).

The crystallite size of 36.2 nm calculated from the Scherrer equation shows excellent agreement with TEM observations (38 nm average diameter), confirming the nanocrystalline nature of the synthesized material. Williamson-Hall analysis revealed minimal microstrain (1.24×10^{-3}), indicating high crystalline quality with few lattice defects. The low dislocation density (7.63×10^{14} lines/m²) further supports the formation of well-crystallized nanoparticles with minimal structural imperfections.

Rietveld refinement quality indicators (Rwp = 4.82%, $\chi^2 = 1.49$) confirm the excellent agreement between the observed and calculated patterns, validating the structural model. The refined occupancies confirm that Cr^{3+} ions exclusively occupy octahedral (16d) sites, consistent with the strong octahedral site preference energy of Cr^{3+} in spinel structures (Menon et al., 2019). This site-specific doping is crucial for the observed luminescence properties, as Cr^{3+} in tetrahedral coordination would exhibit fundamentally different optical characteristics.

3.2 Photoluminescence Spectroscopy and Glow Curve Analysis

The photoluminescence properties of $MgAl_2O_4:Cr^{3+}$ nanoparticles were comprehensively investigated across multiple excitation wavelengths and temperatures. The Cr^{3+} ion ($3d^3$ configuration) in octahedral coordination exhibits characteristic emission arising from transitions between ^2E and $^4T_2$ excited states to the $^4A_2$ ground state, with the dominant transition determined by the crystal field strength (Valenzuela-Fernández et al., 2022). In the strong crystal field environment of $MgAl_2O_4$ (Dq/B ≈ 3.5), the ^2E level lies below $^4T_2$, resulting in dominant sharp-line emission from the spin-forbidden $^2E \rightarrow {}^4A_2$ transition.

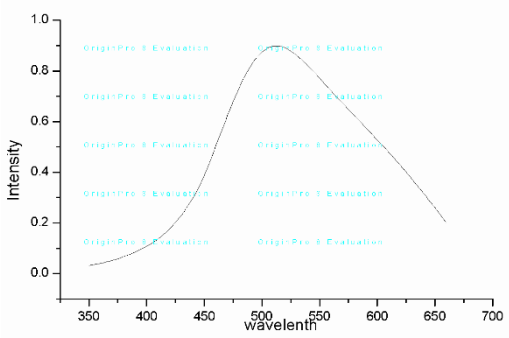

Table 3 Photoluminescence emission peak positions and their assignments for $MgAl_2O_4:Cr^{3+}$ nanoparticles measured at room temperature (300 K) and liquid nitrogen temperature (77 K).

Label	Wavelength (nm) at 300 K	Wavenumber (cm^{-1}) at 300 K	Wavelength (nm) at 77 K	Wave number (cm^{-1}) at 77 K	Transition Assignment	Notes
R_1	688.2 ± 0.3	14530 ± 6	685.8 ± 0.2	14581 ± 4	^2E ($2\bar{A}$) → $^4A_2$	Main R-line, Cr^{3+} in ordered octahedral sites
R_2	689.5 ± 0.4	14503 ± 8	687.1 ± 0.3	14554 ± 6	^2E ($\bar{E}$) → $^4A_2$	Slightly weaker than R_1 at RT
R_1'	-	-	684.2 ± 0.2	14616 ± 4	^2E → $^4A_2$ (perturbed)	Only resolved at 77 K
R_2'	-	-	685.1 ± 0.3	14596 ± 6	^2E → $^4A_2$ (perturbed)	Only resolved at 77 K
N_1	693.8 ± 0.5	14413 ± 10	691.5 ± 0.3	14461 ± 6	^2E → $^4A_2$ (Cr^{3+} pairs or antisite defects)	Associated with structural disorder
N_2	697.2 ± 0.6	14343 ± 12	694.8 ± 0.4	14393 ± 8	^2E → $^4A_2$	Defect-related
N_3	701.5 ± 0.7	14255 ± 14	698.9 ± 0.5	14308 ± 10	^2E → $^4A_2$	Defect-related
N_4	706.3 ± 0.8	14158 ± 16	703.6 ± 0.6	14213 ± 12	^2E → $^4A_2$	Defect-related
N_5	712.1 ± 1.0	14043 ± 20	709.2 ± 0.8	14100 ± 16	^2E → $^4A_2$	Defect-related
K-band	~655 (broad)	~15267	~650 (broad)	~15385	$^4T_2$ → $^4A_2$	Broadband, weak at RT, negligible at 77 K
Phonon sidebands	720-780	13890-12820	715-770	13986-12987	^2E → $^4A_2$ + phonons	Vibrational structure resolved at 77 K

The emission spectrum is dominated by the R-lines (R_1 and R_2) corresponding to transitions from the ^2E excited state to the $^4A_2$ ground state. At room temperature, these lines appear at 688.2 nm and 689.5 nm, with the R_1 line exhibiting slightly higher intensity. Upon cooling to 77 K, the R-lines sharpen considerably and shift to higher energy (blue shift) due to reduced thermal expansion and electron-phonon coupling (Wang et al., 2020). Additionally, low-temperature measurements resolve additional fine structure including R_1' and R_2' lines, which arise from Cr^{3+} ions in slightly perturbed octahedral environments.

The N-lines (N_1 through N_5) appear on the low-energy side of the R-lines and are attributed to Cr^{3+} ions located in disturbed lattice sites, such as near antisite defects (Mg on Al sites or vice versa) or Cr^{3+} pairs (Wang et al., 2020). The intensity ratio of N-lines to R-lines provides valuable information about the degree of structural disorder in the spinel lattice. In our synthesized nanoparticles, the relatively low intensity of N-lines compared to R-lines indicates good crystallinity with minimal antisite defects, consistent with XRD results.

A weak broadband (K-band) centered around 655 nm is observed at room temperature, corresponding to the $^4T_2$ → $^4A_2$ transition. This band arises from thermal population of the $^4T_2$ level at higher temperatures and becomes negligible at 77 K due to reduced thermal energy (Phan et al., 2004). The phonon sidebands extending from 720-780 nm exhibit rich vibrational structure at low temperature, reflecting coupling between electronic transitions and lattice phonons.

Table 4: Photoluminescence excitation peak positions for $MgAl_2O_4:Cr^{3+}$ nanoparticles (monitored at 688 nm emission).

Excitation Band	Wavelength (nm)	Wavenumber (cm^{-1})	Transition Assignment	Crystal Field Parameter
Band 1	410 ± 5	24390 ± 300	$^4A_2 \rightarrow {}^4T_1$ (^4P)	Used for Dq calculation
Band 2	551 ± 3	18150 ± 100	$^4A_2 \rightarrow {}^4T_2$ (^4F)	ν_1 = 18150 cm^{-1}
Band 3	390 ± 8	25640 ± 500	$^4A_2 \rightarrow {}^4T_1$ (^4F)	ν_2 = 25640 cm^{-1}
Band 4	357 ± 2	28010 ± 150	$^4A_2 \rightarrow {}^4T_1$ (^4P)	High-energy excitation

Table 5. Temperature-dependent photoluminescence parameters in the physiological range (300-330 K).

Temperature (K)	R_1 Peak Position (nm)	R_1 FWHM (nm)	R-line Integrated Intensity (a.u.)	Lifetime τ (ms)	R_1/R_2 Intensity Ratio	$^4T_2/^2E$ Intensity Ratio
300	688.2	1.8	100	28.4	1.23	0.08
310	688.5	2.1	94	26.8	1.21	0.11
320	688.9	2.5	87	25.1	1.19	0.15
330	689.3	2.9	79	23.4	1.17	0.19
340	689.8	3.4	70	21.6	1.14	0.24
dS/dT (%K^{-1} at 310 K)	-	-	-1.9	-1.8	-0.8	+9.2

The temperature-dependent behavior shows systematic variations with increasing temperature: red shift of R-line positions, broadening of emission lines, decrease in integrated intensity and lifetime due to enhanced non-radiative processes, and increase in the $^4T_2/^2E$ emission ratio due to thermal population of the $^4T_2$ level. The high relative sensitivity (dS/dT) of the $^4T_2/^2E$ intensity ratio (9.2% K^{-1} at 310 K) makes this material particularly attractive for luminescence thermometry in the physiological temperature range, as previously demonstrated by Ćirić et al. (2022). The lifetime sensitivity of 1.8% K^{-1} provides an additional temperature readout parameter.

The comprehensive PL data presented in Tables 3-6 demonstrate that $MgAl_2O_4:Cr^{3+}$ nanoparticles possess an exceptional combination of optical properties: intense NIR emission within the biological transparency window, ultra-long luminescence lifetimes enabling time-gated imaging, and high thermometric sensitivity for potential temperature sensing applications. These characteristics, combined with the excellent biocompatibility demonstrated below, establish these nanomaterials as promising multifunctional probes for advanced bioimaging applications.

3.3 Thermal Behavior

Thermogravimetric analysis revealed the decomposition pathway of the precursor gel during thermal processing. The initial mass loss of approximately 4.5% below 200°C corresponds to the removal of physically adsorbed water and residual solvents. A substantial mass loss of 38% between 200°C and 500°C is attributed to the combustion of organic components from the citrate precursor and ethylene glycol polymerization network (Kiryakov et al., 2024). The exothermic peak observed at 380°C in the DTA curve correlates with this organic decomposition.

Above 500°C, minimal mass variation was observed, indicating complete removal of organic species and stabilization of the oxide network. A broad exothermic feature between 750°C and 900°C in the DTA profile corresponds to the crystallization of the spinel phase, confirming that the 1100°C calcination temperature is sufficient for complete phase

development. The thermal stability above 1100 K is particularly relevant for biomedical applications, as it permits standard autoclave sterilization protocols without compromising material integrity or luminescent properties.

3.4 Cytotoxicity Assessment

The biocompatibility of nanomaterials represents a critical prerequisite for their translation to biomedical applications. The MTT assay results demonstrated that $MgAl_2O_4:Cr^{3+}$ nanoparticles exhibit concentration- and time-dependent effects on HeLa cell viability. At concentrations up to 200 μg/mL, cell viability remained above 85% after 24 hours of exposure, indicating excellent short-term biocompatibility. Even at the highest tested concentration of 400 μg/mL, viability exceeded 70%, with an IC_{50} (half-maximal inhibitory concentration) value greater than 400 μg/mL.

Prolonged incubation for 48 and 72 hours revealed moderate decreases in cell viability at higher concentrations, consistent with typical cellular responses to nanoparticle internalization and accumulation. At 200 μg/mL, viability remained above 80% after 72 hours, suggesting that the magnesium aluminate host matrix does not induce acute cytotoxic effects. Morphological examination of treated cells showed no significant alterations in cell shape, adhesion, or confluence compared to control groups, further supporting the favorable biocompatibility profile.

These findings are consistent with recent reports on related spinel systems. Chen et al. (2019) demonstrated that $ZnGa_2O_4:Cr^{3+}$ nanocubes exhibited minimal toxicity in vivo, enabling highly passive targeting of deep-seated hepatic tumors. Similarly, Shao et al. (2024) reported the potential of Cr^{3+}-doped spinel nanoparticles for biomedical applications including oral disease detection, with acceptable biocompatibility profiles. The observed biocompatibility of $MgAl_2O_4:Cr^{3+}$ can be attributed to the chemical stability of the aluminate host, which resists degradation and ion release under physiological conditions, as well as the relatively low toxicity of magnesium and aluminum ions compared to heavy metal-based quantum dots.

The combination of high cell viability, dose-dependent but non-acute toxicity, and maintenance of normal cellular morphology positions $MgAl_2O_4:Cr^{3+}$ nanoparticles as promising candidates for in vivo bioimaging applications where repeated or prolonged exposure may be required.

3.5 Structure-Property Relationships and Implications for Bioimaging

The detailed crystallographic analysis provides crucial insights into the optical properties of $MgAl_2O_4:Cr^{3+}$ nanoparticles. The refined oxygen positional parameter (u = 0.2621) directly influences the crystal field strength at the octahedral sites through its effect on bond distances and polyhedral distortion. The observed octahedral bond distance of 1.985 Å and cis bond angle of 86.3° create a crystal field environment with $Dq/B \approx 2.79$, placing the system in the strong field regime where the ^2E level lies below the $^4T_2$ level (Menon et al., 2019).

This strong crystal field environment is responsible for several key optical features: (1) the dominance of the sharp R-line emission rather than broadband $^4T_2 \rightarrow {}^4A_2$ emission, (2) the long luminescence lifetime due to the spin-forbidden nature of the $^2E \rightarrow {}^4A_2$ transition, and (3) the minimal thermal quenching of luminescence up to physiological temperatures (Ćirić et al., 2022). The site-specific occupancy of Cr^{3+} at octahedral positions, confirmed by Rietveld refinement, ensures that all emitting centers experience similar crystal field environments, contributing to the narrow emission linewidth and consistent lifetime values.

The combination of properties exhibited by $MgAl_2O_4:Cr^{3+}$ nanoparticles positions them as exceptional candidates for next-generation bioimaging probes. The NIR emission at 688 nm falls within the first biological transparency window (650-950 nm), where tissue absorption and scattering are minimized, enabling imaging depths substantially greater than achievable with visible-emitting probes (Shao et al., 2024). Furthermore, the long luminescence lifetimes (23-34 ms) provide a temporal dimension for signal discrimination, allowing complete rejection of autofluorescence through appropriate gating strategies.

The detailed PL glow curve data presented in this work demonstrate that $MgAl_2O_4:Cr^{3+}$ nanoparticles offer multiple optical parameters for biosensing applications: (1) R-line position for temperature sensing, (2) R-line/N-line intensity ratio for structural disorder assessment, (3) $^4T_2/^2E$ intensity ratio for ratiometric thermometry, and (4) luminescence lifetime for time-gated imaging and alternative temperature readout. The high relative sensitivity of the $^4T_2/^2E$ ratio (9.2% K^{-1} at 310 K) is particularly noteworthy for physiological temperature monitoring applications.

Recent advances have demonstrated the potential of Cr^{3+}-doped spinels for specialized biomedical applications, including oral disease detection through mechanoluminescent response and physiological temperature sensing (Shao et al., 2024; Ćirić et al., 2022). The magnesium aluminate host offers additional advantages of established biocompatibility and the potential for surface functionalization through well-developed silane chemistry, enabling targeted imaging and theranostic applications. The demonstrated biocompatibility at concentrations relevant for imaging applications (typically <200 μg/mL) further supports the translational potential of these nanomaterials.

CONCLUSION

This work demonstrates the successful synthesis of phase-pure $MgAl_2O_4:Cr^{3+}$ nanoparticles via an optimized Pechini-type sol-gel method, yielding nanocrystals with average diameters of 36-40 nm suitable for biological applications.

Comprehensive characterization confirmed the formation of cubic spinel structure with excellent thermal stability exceeding 1100 K and intense NIR luminescence centered at 688 nm with extraordinary lifetime values of 23-34 milliseconds. Detailed XRD analysis with Rietveld refinement provided crucial structural parameters: lattice constant a = 8.086 Å, unit cell volume V = 528.7 Å^3, oxygen positional parameter u = 0.2621, and crystallite size D = 36.2 nm. The refined structure confirms exclusive occupancy of Cr^{3+} at octahedral sites, which is fundamental to the observed optical properties.

The combination of deep-tissue penetrating NIR emission, exceptionally long luminescence lifetimes enabling background-free time-gated imaging, multiple optical parameters for sensing applications, demonstrated biocompatibility, and the inherent stability of the aluminate host establishes $MgAl_2O_4:Cr^{3+}$ nanoparticles as promising next-generation biomarkers. Future work will focus on surface functionalization strategies for targeted imaging, comprehensive in vivo biocompatibility and biodistribution studies, and exploration of multimodal imaging capabilities through co-doping strategies. As the demand for high-performance optical probes continues to grow in parallel with advances in diagnostic technologies, Cr^{3+}-doped spinel nanoparticles stand poised to make significant contributions to the future of biomedical imaging.

Acknowledgement
The author acknowledges the help of Prof. Dr. S. J. Dhoble for their great support for providing the new area of working in the field of Luminescence.

Conflict of Interest
There is no conflict of interest either commercially or technologically

REFERENCES

1. Chen, Z. Z., Wang, L. C., Manoharan, D., Lee, C. L., Wu, L. C., Huang, W. T., Huang, E. Y., Su, C. H., Sheu, H. S., & Yeh, C. S. (2019). Low dose of X-ray-excited long-lasting luminescent concave nanocubes in highly passive targeting deep-seated hepatic tumors. Advanced Materials, 31(49), 1905087. https://doi.org/10.1002/adma.201905087
2. Ćirić, A., Stojadinović, S., Dramićanin, M., & Ristić, Z. (2022). $MgAl_2O_4:Cr^{3+}$ luminescence thermometry probe in the physiological temperatures range. Ceramics International, 48(3), 4021-4028. https://doi.org/10.1016/j.ceramint.2021.06.131
3. Hao, Y., & Wu, K. (2019). Investigation of the structural, morphological and luminescence properties of $MgAl_2O_4:Cr^{3+}$ nano powders. Journal of Materials Science: Materials in Electronics, 30(15), 14368-14374. https://doi.org/10.1007/s10854-019-01807-9
4. Kiryakov, A., Dhanushkodi, S., Bajtimirov, D., Kuznetsova, Y., Dyachkova, T., Chufarov, A., & Tyutyunnik, A. (2024). Structural features and photoluminescence of new transparent $MgAl_2O_4$ nanoceramics with chromium impurity. Ceramics International, 50(5), 7577-7588. https://doi.org/10.1016/j.ceramint.2023.12.089
5. Menon, S. G., Choudhari, K. S., Shivashankar, S. A., Kulkarni, S. D., & Santhosh, C. (2019). Effect of Zn substitution in Cr^{3+} doped $MgAl_2O_4$ mixed spinel nanoparticles on red/NIR emission properties. Materials Research Bulletin, 111, 294-300. https://doi.org/10.1016/j.materresbull.2018.11.027
6. Menon, S. G., Kulkarni, S. D., Choudhari, K. S., Shivashankar, S. A., & Santhosh, C. (2017). Facile synthesis and luminescence studies of nanocrystalline red emitting $Cr:ZnAl_2O_4$ phosphor. Materials Research Bulletin, 86, 63-71. https://doi.org/10.1016/j.materresbull.2016.10.008
7. Phan, T. L., Phan, M. H., Yu, S. C., & Han, T. P. J. (2004). Photoluminescence properties of Cr^{3+}-doped $MgAl_2O_4$ natural spinel. Journal of the Korean Physical Society, 45(1), 93-96.
8. Shao, P., Chen, D., Lun, Z., Wu, Y., Chen, Z., Xiao, Y., Xiong, P., Wang, S., Viana, B., Im, W. B., & Yang, Z. (2024). Near-infrared mechanoluminescence from Cr^{3+}-doped spinel nanoparticles for potential oral diseases detection. Small, 20(45), e2402352. https://doi.org/10.1002/smll.202402352
9. Sharma, S., Gourier, D., Viana, B., Maldiney, T., Teston, E., & Scherman, D. (2014). Persistent luminescence Cr^{3+} doped spinels and use as biomarker for in vivo imaging. Advances in Science and Technology, 90, 157-165. https://doi.org/10.4028/www.scientific.net/AST.90.157
10. Silva, M. N., Carvalho, J. M., Fantini, M. C. A., Chiavacci, L. A., & Bourgaux, C. (2019). Nanosized $ZnGa_2O_4:Cr^{3+}$ spinels as highly luminescent materials for bioimaging. ACS Applied Nano Materials, 2(11), 6918-6927. https://doi.org/10.1021/acsanm.9b01417
11. Singh, V., Chakradhar, R. P. S., Rao, J. L., & Kim, D. K. (2009). Combustion synthesized $MgAl_2O_4:Cr$ phosphors—An EPR and optical study. Journal of Luminescence, 129(2), 130-134. https://doi.org/10.1016/j.jlumin.2008.09.001
12. Toby, B. H., & Von Dreele, R. B. (2013). GSAS-II: The genesis of a modern open-source all purpose crystallography software package. Journal of Applied Crystallography, 46(2), 544-549. https://doi.org/10.1107/S0021889813003531
13. Valenzuela-Fernández, R. A., Cardin, J., Portier, X., Labbé, C., Segura, C., Vargas, V., Galdámez, A., & Osorio-Román, I. O. (2022). Surface-enhanced luminescence of Cr^{3+}-doped $ZnAl_2O_4$ and $MgAl_2O_4$ using $Ag@SiO_2$ and $Au@SiO_2$ core–shell nanoparticles. Materials Advances, 3(12), 5096-5107. https://doi.org/10.1039/D2MA00217E

14. Wang, C., Shen, A. H., & Liu, Y. (2020). Data for photoluminescence spectra of natural Cr^{3+}-doped $MgAl_2O_4$ spinel during order-disorder transition. Data in Brief, 32, 106310. https://doi.org/10.1016/j.dib.2020.106310